Available online at www.sciencedirect.com

ScienceDirect

Ceramics International 40 (2014) 2697–2706

CERAMICS INTERNATIONAL

www.elsevier.com/locate/ceramint

Synthesis and characterization of chlorapatite–ZnO composite nanopowders

Bahman Nasiri-Tabrizi, Abbas Fahami*

Materials Engineering Department, Najafabad Branch, Islamic Azad University, Najafabad, Isfahan, Iran

Received 16 September 2013; received in revised form 11 October 2013; accepted 12 October 2013
Available online 22 October 2013

Abstract

The influence of zinc oxide content on the formation of chlorapatite-based composite nanopowders in the mechanically alloyed $CaO–CaCl_2–P_2O_5–ZnO$ system was studied. To mechanosynthesize composite nanopowders, different amounts of hydrothermally synthesized zinc oxide nanoparticles (0–10 wt%) were mixed with ingredients and then were mechanically activated for 5 h. Results showed that in the absence of zinc oxide, high crystalline chlorapatite nanopowder was obtained after 5 h of milling. In the presence of 4 and 7 wt% zinc oxide, the main product of milling for 5 h was chlorapatite–zinc oxide composite nanopowder. On increasing the zinc oxide content to 10 wt%, composite nanopowder was not formed due to improper stoichiometric ratio of the reactants. The crystallite size, lattice strain, volume fraction of grain boundary, and crystallinity degree of the samples fluctuated significantly during the milling process. In the presence of 7 wt% zinc oxide, the crystallite size and crystallinity degree reached 51 ± 2 nm and $79 \pm 2\%$, respectively. During annealing at 900 °C for 1 h, the crystallization of composite nanopowder occurred and as a result the crystallinity degree rose sharply to $96 \pm 3\%$. In addition, the crystallite size increased to 77 ± 2 nm after annealing at 900 °C. According to SEM and TEM images, the composite nanopowder was composed of both ellipse-like and polygonal particles with a mean size of about 98 nm.

Keywords: D. ZnO; Chlorapatite-based composite; Mechanosynthesis; SEM/TEM images; Structural features

1. Introduction

Hydroxyapatite (HAp, $Ca_{10}(PO_4)_6(OH)_2$) is the main inorganic constituent of bones and teeth [1]. Synthetic hydroxyapatite (s-HAp) has long been recognized as one of the most important bioceramics in biomedical applications due to its chemical and biological similarity to the mineral phase of human bone [2]. However, s-HAp has an intrinsically high dissolution rate in a biological system, poor corrosion resistance in an acidic environment, and poor chemical stability at high temperatures [3]. Therefore, the modification of HAp has been done by the substitution of chemical species found in the natural bone [4].

In apatite formula ($M_{10}(XO_4)_6Y_2$), M can be substituted by a large number of various ions like Ca^{2+}, Mg^{2+}, Sr^{2+}, Ba^{2+}, Mn^{2+}, Fe^{2+}, Zn^{2+}, Cd^{2+}, Pb^{2+}, H^+, Na^+, K^+, Al^{3+} and so on. In addition, XO_4 can be replaced by PO_4^{3-}, AsO_4^{3-}, VO_4^{3-}, SO_4^{3-}, CO_4^{3-}, SiO_4^{3-}, while Y can be substituted by several anions like OH^-, F^-, Cl^-, Br^-, O^{2-}, and CO_3^{2-} [5,6]. It has been found that these modifications influence the chemical and physical properties as well as bone bonding capability of s-HAp after implantation [7]. In order to reduce the dissolution rate of HAp, the substitution of OH^{-1} groups by F^{-1} ions is very effective and it causes an increase in crystallinity degree, a decrease in crystal strain, and an increase in thermal and chemical stability [8,9]. Also, it has been reported that the substitution of Cl^{-1} ions in HAp lattice led to the formation of an acidic environment on the surface of bone which resulted in the activation of the osteoclasts in the bone resorption process [10]. This ionic modification has been carried out by hydrothermal treatments [11], aqueous precipitation method [7], and mechanochemical process [12]. The advantage of the wet process is that the byproduct is almost water and as a result the probability of contamination during the process is very low, while the dry process has the benefit of high reproducibility and low processing cost [13,14]. On the other hand, the incorporation of bioinert ceramics into the calcium phosphates improves their mechanical properties [15,16]. An ideal reinforcing material for the calcium phosphate-based composites has not yet been identified.

*Corresponding author. Tel.: +98 3114437009; fax: +98 3312291008.
E-mail addresses: ab.fahami@gmail.com, a.fahami@hotmail.com (A. Fahami).

0272-8842/$ - see front matter © 2013 Elsevier Ltd and Techna Group S.r.l. All rights reserved.
http://dx.doi.org/10.1016/j.ceramint.2013.10.053

Consequently, synthetic calcium phosphate-based composites available for clinical use are under continuous change [17]. According to literature, zinc is a vital trace element in a variety of cellular processes including DNA synthesis, behavioral responses, reproduction and virility, bone formation, bone growth and wound healing [18]. Furthermore, zinc plays an important role in gene expression and in the regulation of cellular growth [19]. The addition of zinc to the deficient diets resulted in a stimulation of both bone growth and mineralization [20]. To the best of our knowledge, an extensive research on the production of HAp–ZnO composites has a rather short history. Recently, it has been found that HAp/ZnO-nanorod composite coatings may have great potential in osseointegration coating applications [21]. Hence, synthesis and characterization of chlorapatite–zinc oxide (CAp–ZnO) composite nanopowders by a novel facile mechanochemical process provided the main incentive for current research.

In the present study, the effect of ZnO content on mechanosynthesis of CAp–ZnO composite nanopowders was investigated. To evaluate the influence of thermal treatment on the crystallization of composite nanopowder, the product was annealed at 900 °C for 1 h. The structural features and morphological characteristics of the composite nanopowders were determined. The knowledge obtained in this study will contribute to produce new valuable biomaterials and to provide appropriate circumstances for the large scale synthesis of CAp–ZnO composite nanopowders.

2. Materials and methods

2.1. Hydrothermal synthesis of ZnO nanopowder

All chemicals were of analytical grade and were used without further purification. To prepare the precursor solutions, zinc nitrate hexahydrate ($Zn(NO_3)_2$ $6H_2O$; 0.05 M) was mixed with methenamine ($(CH_2)_6N_4$; 0.1 M), while their volume ratio was 1:1. After that, the mixed solution was sonicated for 30 min with a rotational speed of 1000 rpm. Then, 400 mL of clear precursor solution was transferred into a Teflon-lined autoclave (500 mL) and maintained at 95 °C for 2 h. The experimental output was washed three times with distilled water and ethanol, and subsequently dried at room temperature. The synthesized powder was used as a reinforcing material in the mechanosynthesis of composite nanopowders.

2.2. Mechanosynthesis of CAp–ZnO composite nanopowders

Fig. 1 shows a schematic overview of the production process. The raw materials were calcium oxide (CaO, Merck), calcium chloride ($CaCl_2$, Merck), and phosphorous pentoxide (P_2O_5, Merck). The mole ratio of calcium to phosphorous was kept constant at 1.67 for all the samples. Milling was carried out in a high energy planetary ball mill using tempered chrome steel vials (vol. 125 mL) and balls (20 mm in diameter) at a rotational speed of 600 rpm and a ball-to-powder weight ratio of 20:1. To synthesize CAp–ZnO composite nanopowders, the different amounts of hydrothermally synthesized ZnO nanoparticles (0, 4, 7, and 10 wt%) were mixed with appropriate amounts of CaO, P_2O_5, and $CaCl_2$ according to the following reaction. Afterwards, the mixed powders were mechanically activated for 5 h without using any process control agent (PCA).

$$9CaO + CaCl_2 + 3P_2O_5 + ZnO \rightarrow Ca_{10}(PO_4)_6Cl_2 + ZnO \quad (1)$$

The mechanosynthesized composite nanopowder was annealed 900 °C for 1 h. The heating rate from room temperature to the desired temperature was fixed at 10 °C min^{-1}.

2.3. Characterization techniques

The phase compositions of the products were examined by X-ray diffraction (Philips X-ray diffractometer (XRD), *Cu–K_α* radiation, 40 kV, 30 mA and 0.02° s^{-1} step scan).

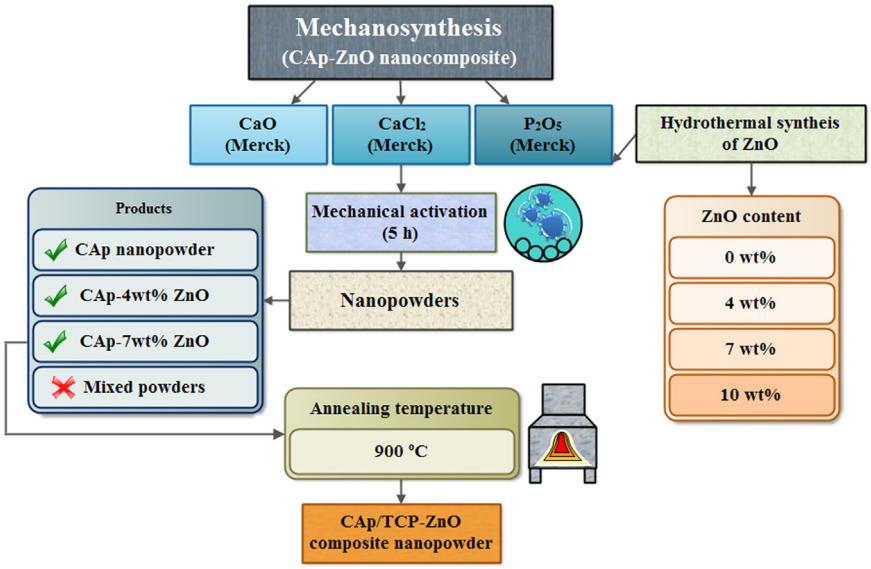

Fig. 1. A schematic overview of the production process.

For qualitative analysis, XRD patterns were recorded in the interval $10^\circ \le 2\theta \le 90^\circ$ at scan speed of $1^\circ\ min^{-1}$. The XRD profiles were compared to standards compiled by the Joint Committee on Powder Diffraction and Standards (JCPDS), which involved card #27-0074 for CAp, #003-1123 for CaO, #005-0586 for $CaCO_3$, #01-1079 for $Ca(OH)_2$, #001-1104 for $CaCl_2\ H_2O$, #011-0232 for $Ca_4P_2O_9$, #036-1451 for ZnO, and #09-0169 for β-TCP. To determine the crystallite size and lattice strain of the specimens, Williamson-Hall method was applied [22].

$$B\ \cos\ \theta = \frac{0.9\lambda}{D} + \eta\ \sin\ \theta \quad \text{(I)}$$

where λ, D, η and θ are the wavelength of the X-ray used (0.154056 nm), crystallite size, internal micro-strain and the Bragg angle (°), respectively. Note that B in the above equation is the peak width (in radians) after subtracting the peak width due to instrumental broadening from the experimentally recorded profile. Therefore, when $B\cos\theta$ was plotted against $\sin\theta$, straight lines were obtained for samples with the slope as η and the intercept as $0.9\lambda/D$.

If we assume that a crystallite is a sphere of diameter D surrounded by a shell of grain boundary with thickness t, the volume fraction of grain boundary (f) is approximately [23]:

$$f = 1 - \left[\frac{D}{(D+t)}\right]^3 \quad \text{(II)}$$

To determine the values of f, the obtained values of crystallite size was replaced with D under the assumption of $t=1$ nm. In addition, the crystallinity degree (X_c) of nanopowders was estimated by taking the sum total of relative intensities of individual characteristic peaks according to the following equation [24]:

$$X_c = \frac{Sum(I_1 : I_n)_{CAp}}{Sum(I_1 : I_n)_{Standard}} \times 100 \quad \text{(III)}$$

where $I_1{:}I_n$ is the total of relative intensities of characteristic peaks of CAp for both the synthesized powders and standard.

The lattice parameters (a, b, and c) can be evaluated from the following relation:

$$\frac{1}{d^2} = \frac{4}{3}\frac{h^2+hk+k^2}{a^2} + \frac{l^2}{c^2} \quad \text{(IV)}$$

where h, k, and l are the Miller indices [25].

The unit cell volume (V) of CAp was determined using the following equation [26]:

$$V = (3a^2c)(\sin\ 60^\circ) \quad \text{(V)}$$

The functional groups of the composite nanopowders were measured using Fourier transformed infrared (FT-IR) transmission spectroscopy (Perkin Elmer Spectrum 65 FT-IR Spectrometer, USA) in the range of 4000–400 cm^{-1}. The crushed samples were diluted 100 fold with KBr powder and the background noise was corrected with pure KBr data. All spectra were recorded at ambient temperature. Scanning electron microscopy (SEM, LEO 435VP, UK), operated at 18 kV acceleration voltage, was utilized for microstructural examination. Also, the hydrothermally synthesized ZnO nanoparticles were examined on a field emission scanning electron microscope (FE-SEM Hitachi S1831) that operated at the acceleration voltage of 15 kV. Moreover, a more detailed morphological analysis was performed using TEM (Philips CM10, Eindhoven, The Netherlands) that operated at the acceleration voltage of 100 kV.

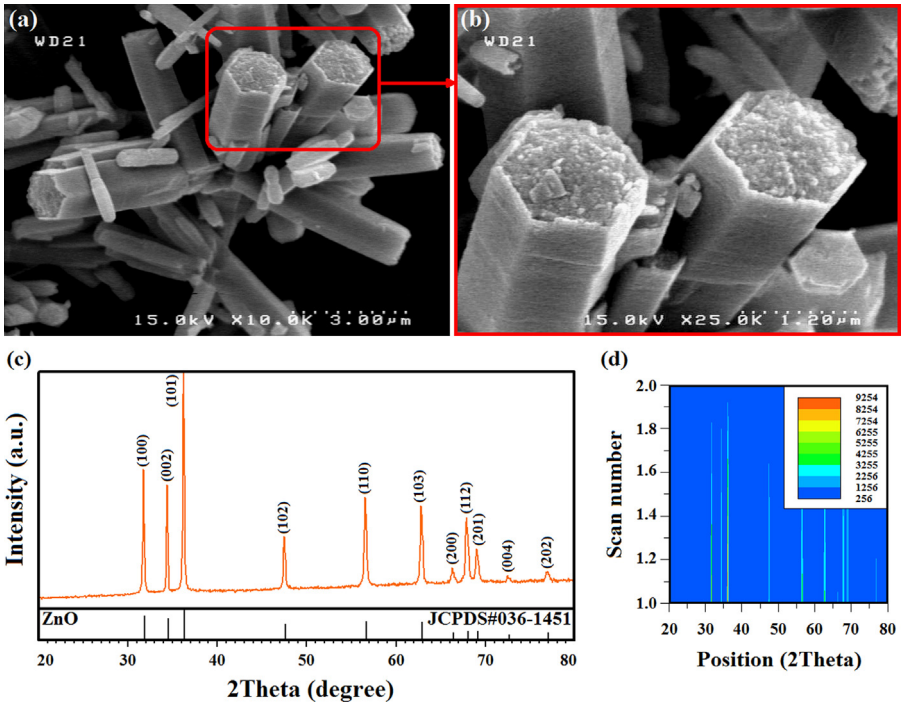

Fig. 2. (a, b) FE-SEM images (c) XRD profile, and (d) isolines view of the hydrothermally synthesized ZnO nanoparticles.

3. Results and discussion

3.1. Characterization of ZnO nanopowder

Fig. 2a and b show FE-SEM images of hydrothermally synthesized ZnO nanoparticles. According to this figure, the synthesized powder had a hexagonal columnar structure. As shown at higher magnification, ZnO nanorods had an average diameter of rods ranging from 200 nm to 1.5 μm. In addition, the arm length of nanorods ranged from 1 to 3 μm. Fig. 2c shows that the hydrothermally synthesized powder was high purity ZnO which had a hexagonal structure (space group P63mc). Fig. 2d shows the isolines view of the hydrothermally synthesized ZnO nanoparticles. This plot displays the overlapping range of all scan data in an isoline (contour lines) graph and is commonly used to show multiple scans as stemming from a non-ambient experiment or a stress measurement [27]. This approach has also been used to appraise the fraction of crystalline phase [28]. As shown in this graph, overlapping range of all scan data was very low. This suggests that the synthesized ZnO nanopowder had high crystalline structure.

3.2. Characterization of CAp–ZnO composite nanopowders

3.2.1. Phase analysis

Fig. 3 shows the XRD patterns of the powder mixture in the absence and presence of different amounts of ZnO nanopowder (0–10 wt%) after mechanical activation for 5 h. According

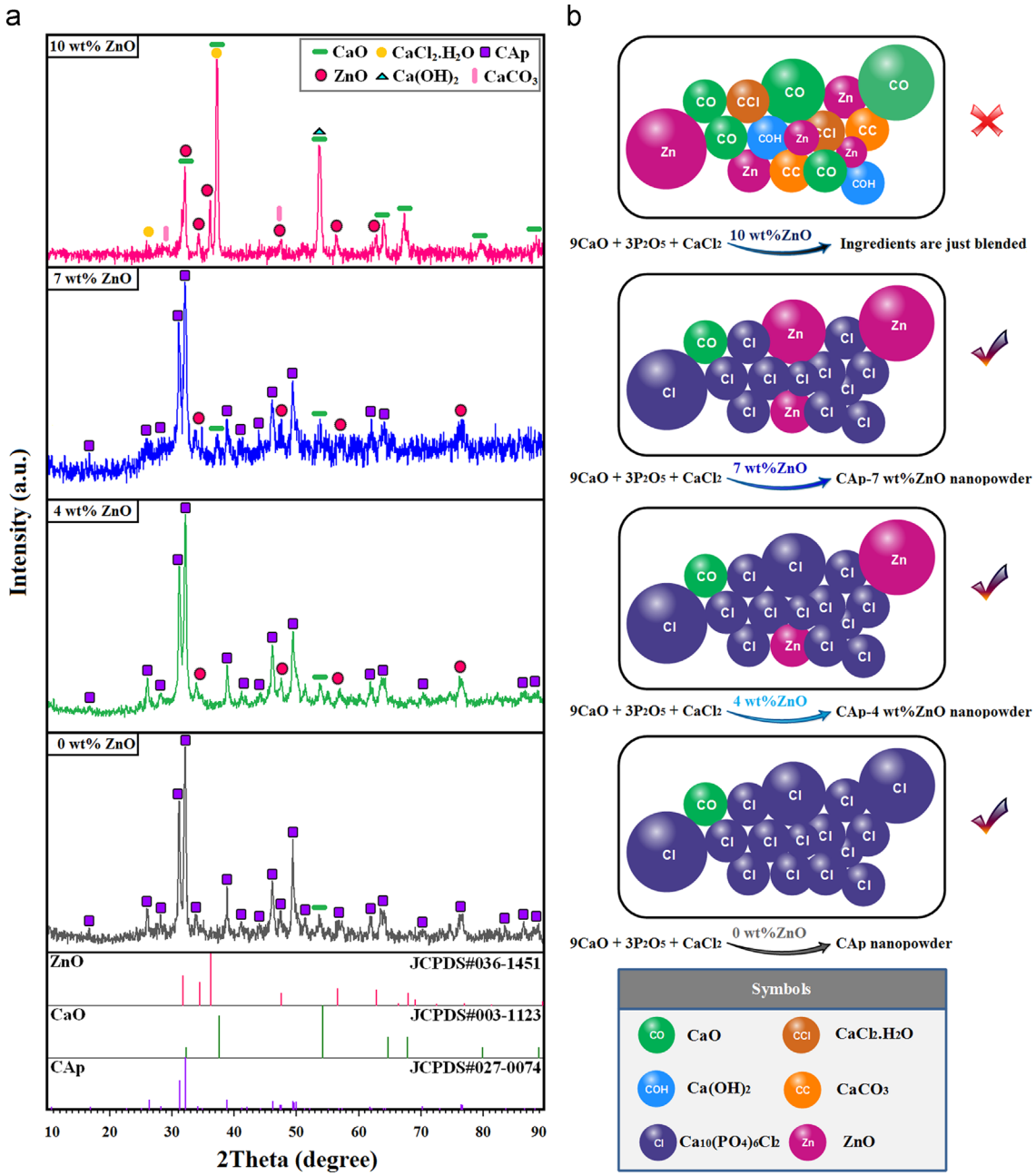

Fig. 3. (a) XRD patterns and (b) schematic views of the powder mixture in the absence and presence of different amounts of ZnO nanopowder (0–10 wt%) after mechanical activation for 5 h.

to Fig. 3a, in the absence of ZnO, all the peaks belonging to the ingredients disappeared and only those corresponding to CAp were detectable after 5 h of milling. Of course, a weak peak corresponding to CaO was identified. As shown in the schematic view (Fig. 3b), in the absence of ZnO the phase compositions were CAp and CaO after 5 h of milling. With the addition of 4 wt% ZnO, milling for 5 h resulted in the formation of CAp–4 wt% ZnO composite nanopowder. Similar to the previous sample, an extra peak corresponding to CaO was diagnosed. In this sample, the phase compositions were CAp, ZnO and CaO after 5 h of milling. On increasing the ZnO content to 7 wt%, a CAp–7 wt% ZnO composite nanopowder was formed. The presence of CaO in these specimens could be a trace of the original product of the original reaction used to produce the composite nanopowder [29]. Similarly, undesirable compounds such as NH^{4+} ions and NO_3 group were detected in the wet chemical synthesis of CAp nanostructures [11,30]. When the ZnO content reached 10 wt%, CAp–ZnO composite was not formed. This behavior can be attributed to the stoichiometric proportionality between the calcium and phosphorus reagents. It has been found that [31], mechanochemical synthesis of calcium phosphate-based composites was influenced dramatically by the mixing ratio. In the mechanically alloyed $CaO–CaCl_2–P_2O_5–ZnO$ system, the mechanochemical behavior was affected by the presence of P_2O_5 in the reaction mixture and can be explained considering the hygroscopic nature of P_2O_5 (reaction (2)).

$$3P_2O_5 + 9H_2O \rightarrow 6H_3PO_4 \quad \Delta G_{298\ K} = -493.081\ \text{kJ}, \quad \Delta H_{298\ K} = -586.317\ \text{kJ} \tag{2}$$

On increasing the ZnO content to ≥ 10 wt%, the weight percent (wt%) of calcium and phosphorus reagents declined significantly and consequently no mechanochemical reaction occurred after 5 h of milling due to the improper stoichiometric ratio of reactants. Under these conditions, the particle size reduction may have occurred. According to the schematic view (Fig. 3b), CaO, $CaCO_3$, $Ca(OH)_2$, $CaCl_2.H_2O$, and ZnO were the main components of the composite structures in the presence of 10 wt% ZnO.

3.2.2. Structural features

The crystallite size, lattice strain, volume fraction of grain boundary, and the crystallinity degree of the powder mixture in the absence and presence of 4 and 7 wt% ZnO after 5 h of milling are shown in Fig. 4. It is obvious that the structural features of the nanopowders fluctuated during the milling process. In the absence of ZnO, the crystallite size and lattice strain of the sample were 28 ± 2 nm and 0.0108 ± 0.0005, respectively (Fig. 4a and b). With the addition of 4 wt% ZnO, the crystallite size increased and reached a maximum of

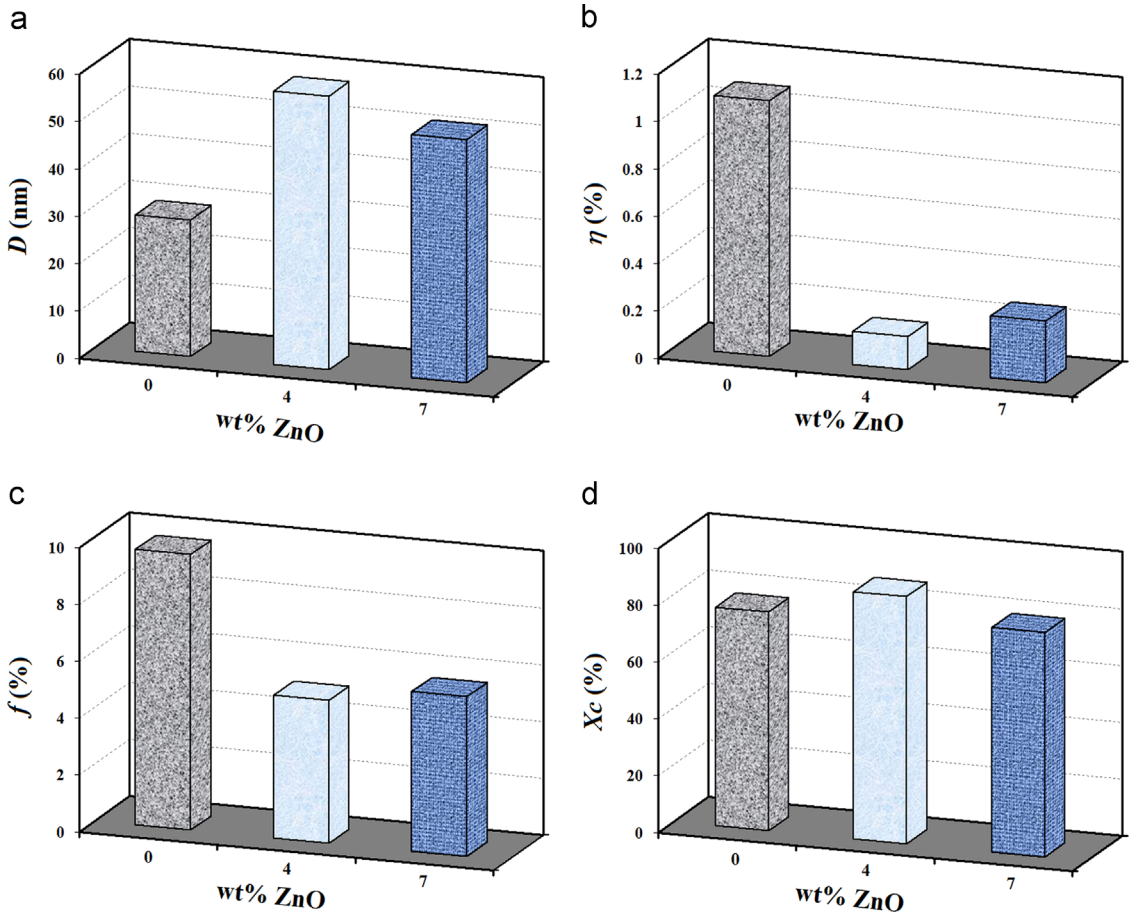

Fig. 4. (a) Crystallite size, (b) lattice strain, (c) volume fraction of grain boundary, and (d) the crystallinity degree of the powder mixture in the absence and presence of 4 and 7 wt% ZnO after 5 h of milling.

57 ± 3 nm. In contrast, the lattice strain declined dramatically to 0.0014 ± 0.00007. Further increasing the ZnO content to 7 wt% led to a slight decrease in the crystallite size and a minor increase in the lattice parameter. According to the obtained data, the volume fraction of grain boundary in the absence of ZnO was higher than the milled specimens in the presence of 4 and 7 wt% ZnO (Fig. 4c). In the absence of ZnO, this value was 0.097 ± 0.004 and reached a minimum of 0.052 ± 0.002 in the presence of 4 wt% ZnO. In accordance with Fig. 4d, the milled powder in the presence of 4 wt% ZnO had the highest degree of crystallinity (87 ± 4%) among the samples. This suggests that the addition of appropriate amounts of ZnO can improve the crystallinity degree of CAp-based composites. It has been found that apatites with high crystallinity degree show little or no activity towards bioresorption and are insoluble in physiological environment [32]. Hence, the synthesized composite nanopowders especially in the presence of 4 wt% ZnO can be considered in biomedical applications.

Fig. 5 shows the lattice parameters and unit cell volume of CAp as a function of ZnO content. For the standard sample (JCPDS#27-0074), *a*-axis and *c*-axis values are 9.6420 and 6.7756 Å, respectively. Besides, the unit cell volume of CAp is 1636.567 Å^3. Based on the obtained data, these values in the absence and presence of ZnO fluctuated during the milling process. In the absence of ZnO, the *a*-axis and *c*-axis values reached around 9.6250 and 6.8191 Å, respectively. Also, the unit cell volume of CAp increased to 1641.2714 Å^3. With the addition of 4 wt% ZnO, an improvement in the lattice structure of CAp occurred and as a result the unit cell volume of CAp was close to the standard value. Further increasing the ZnO content to 7 wt% led to a substantial increase in the unit cell volume. The difference in unit cell dimensions can probably be ascribed to the lattice distortion of CAp during the milling process. Therefore, it can be concluded that the unit cell dimensions of CAp were notably influenced by the ZnO content.

3.2.3. FT-IR analysis

The FT-IR spectra of the powder mixture in the absence and presence of 4 and 7 wt% ZnO after 5 h of milling are shown in Fig. 6. The characteristic groups of the products including PO_4^{3-}, CO_3^{2-}, and Zn–O are visible in 4000–400 cm^{-1} region in the FT-IR spectra [12,31,33–35]. In the absence of ZnO, two bands belonging to the vibration of the adsorbed water in apatites were detected at 3432.23 and 1642.61 cm^{-1} [12]. Similarly, these bands were identified for the milled samples in the presence of 4 and 7 wt% ZnO. In these spectra, the absence of the bands at 630 and 3568 cm^{-1} corresponding to OH^- liberation mode and the appearance of a band at 733 cm^{-1} showed the formation of CAp [33]. The stretching vibration of the Zn–O appeared as a broad band in the range of 700–500 cm^{-1} [34]. In the absence of ZnO, the bands at 1091.7 and 1047.05 cm^{-1} ascribed to ν_3 PO_4, the band at 960.45 cm^{-1}

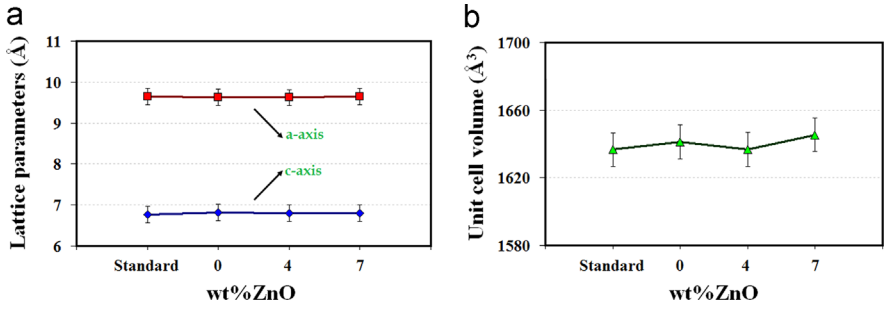

Fig. 5. (a) Lattice parameters and (b) unit cell volume of CAp as a function of ZnO content.

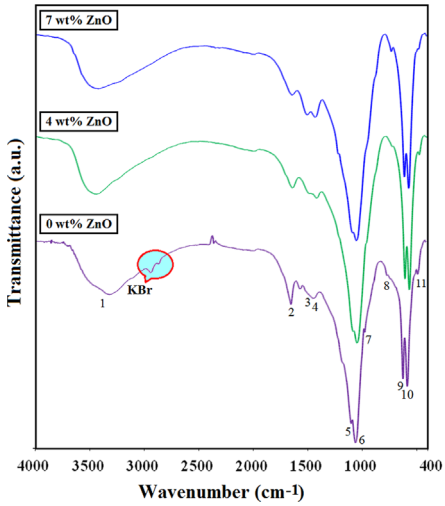

No.	Assignment	Infrared frequency (cm^{-1})		
		0 wt% ZnO	4 wt% ZnO	7 wt% ZnO
1	H_2O	3432.23	3438.88	3411.31
2	H_2O	1642.61	1638.92	1642
3	$\upsilon_3(CO_3^{2-})$	1495.7	1495.7	1510.8
4	$\upsilon_3(CO_3^{2-})$	1414.9	1416.32	1426.35
5	$\upsilon_3(PO_4^{3-})$	1091.7	1091.7	1091.7
6	$\upsilon_3(PO_4^{3-})$	1047.05	1047.37	1048.12
7	$\upsilon_1(PO_4^{3-})$	960.45	960.45	955.4
8	$\upsilon_2(CO_3^{2-})$	-	-	879.66
9	$\upsilon_4(PO_4^{3-})$	607.38	607.76	608.13
10	$\upsilon_4(PO_4^{3-})$	567.95	567.86	568.30
11	$\upsilon_2(PO_4^{3-})$	473.30	475.74	475.74
12	Zn–O	700–500	700–500	700–500

Fig. 6. FT-IR spectra of the powder mixture in the absence and presence of 4 and 7 wt% ZnO after 5 h of milling.

belonged to ν_1 PO_4, the bands at 607.38 and 567.95 cm^{-1} result from ν_4 PO_4, and the band at 473.30 cm^{-1} comes from ν_2 vibration of the PO_4^{3-} group [31]. With the addition of 4 and 7 wt% ZnO, the phosphate groups had fluctuated slightly during the milling process. In all the spectra, the appearance of the bands at 1495.7 and 1414.9 cm^{-1} corresponding to carbonated groups indicated that the composite nanopowders contained some CO_3^{2-} groups in PO_4^{3-} sites of apatite lattice (B-type substitution) which can be very helpful in orthopedic applications [35]. Based on FT-IR spectra, the mechanosynthesized CAp–ZnO composite nanopowders had high chemical purity which is vital in biomedical applications.

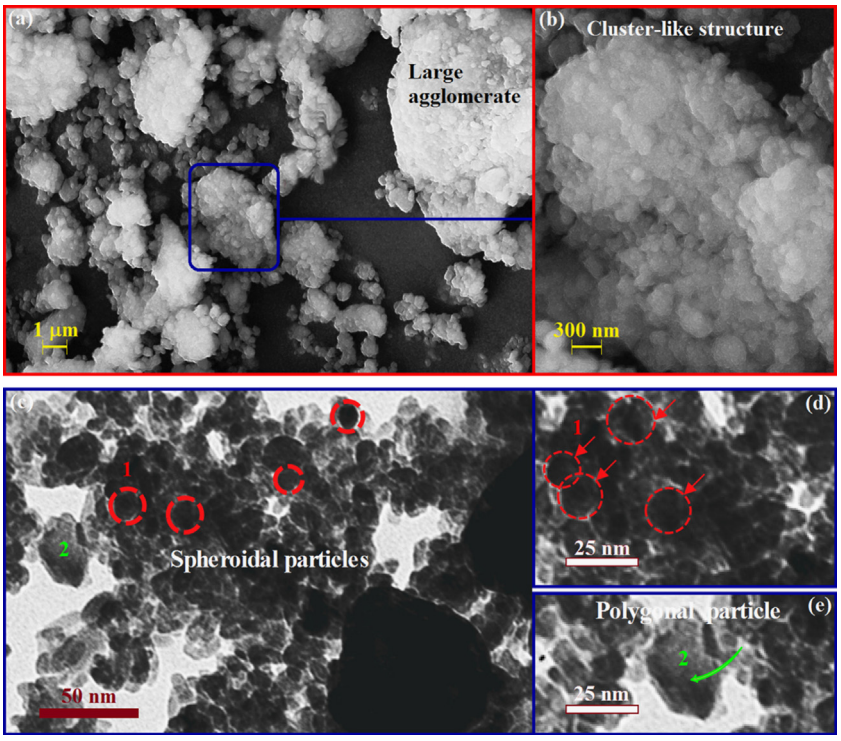

Fig. 7. (a, b) SEM and (c–e) TEM images of CAp nanopowder in the absence of ZnO.

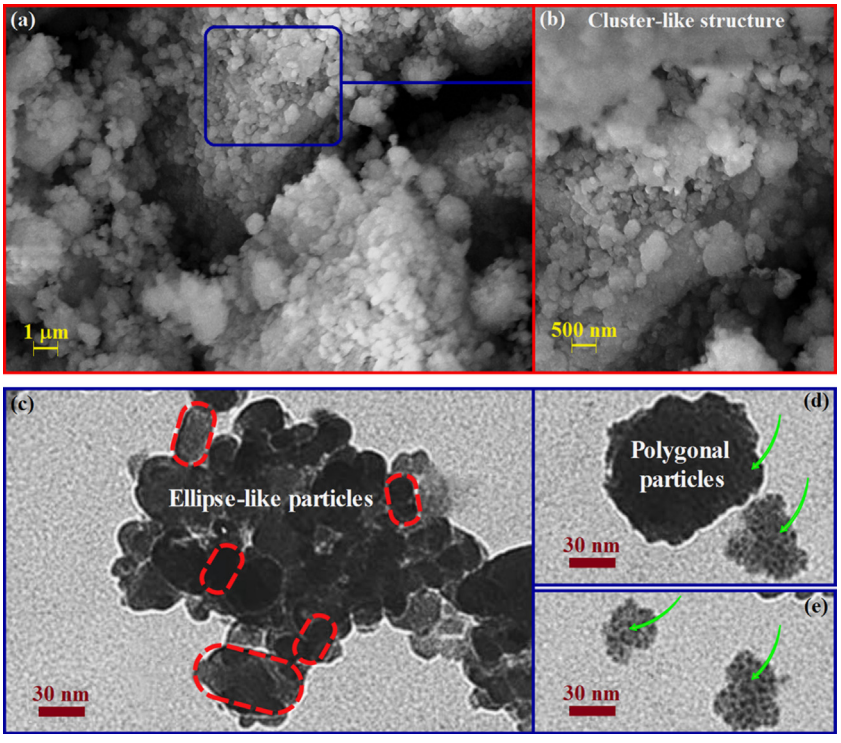

Fig. 8. (a, b) SEM and (c–e) TEM images of CAp–7 wt% ZnO composite nanopowder.

3.2.4. SEM and TEM observations

Fig. 7 shows SEM and TEM images of CAp nanopowder in the absence of ZnO. According to this figure, the synthesized nanopowder had high tendency to agglomerate owing to its relatively large specific surface which were associated with van der Waals interactions [36]. From mechanochemistry point of view, when two adjacent primary particles collide, the coalescence may occur on the premise that these two particles share a common crystallographic orientation. Accordingly, two primary particles attach to each other and combine into a secondary one. Since the sizes of the secondary particles are still very small, it is reasonable that they will continue to collide and coalesce which may ultimately lead to the agglomeration. In SEM images of Fig. 7a and b, CAp nanopowder had a cluster-like structure which was composed of several fine particles with an average size of about 95 nm. In accordance with the TEM images, the cluster-like structure was comprised of both spheroidal and polygonal particles. The morphological features of a CAp–ZnO composite nanopowder are presented in Fig. 8. Similar to CAp nanopowder, a cluster-like structure was formed in the presence of 7 wt% ZnO after 5 h of milling. According to this figure, the mean particle size of the mechanosynthesized composite nanopowder with ellipse-like and polygonal morphologies was about 98 nm. Based on these observations, the addition of ZnO nanopowder as a second phase had an inhibitory role in reducing the particle size.

3.3. Thermal treatment

The effect of thermal treatment at 900 °C for 1 h on the crystallization behavior of CAp–ZnO composite nanopowder is shown in Fig. 9. From XRD profile in Fig. 9a, a substantial rise in the peak intensities and a significant reduction in breadth of the fundamental diffraction peaks are obvious. This behavior suggests that the crystallization of the composite nanopowder occurred during annealing at 900 °C. Besides, annealing at 900 °C led to the slight decomposition of CAp to tricalcium phosphate (β-TCP), tetracalcium phosphate ($Ca_4P_2O_9$), and hydrochloric acid according to the following

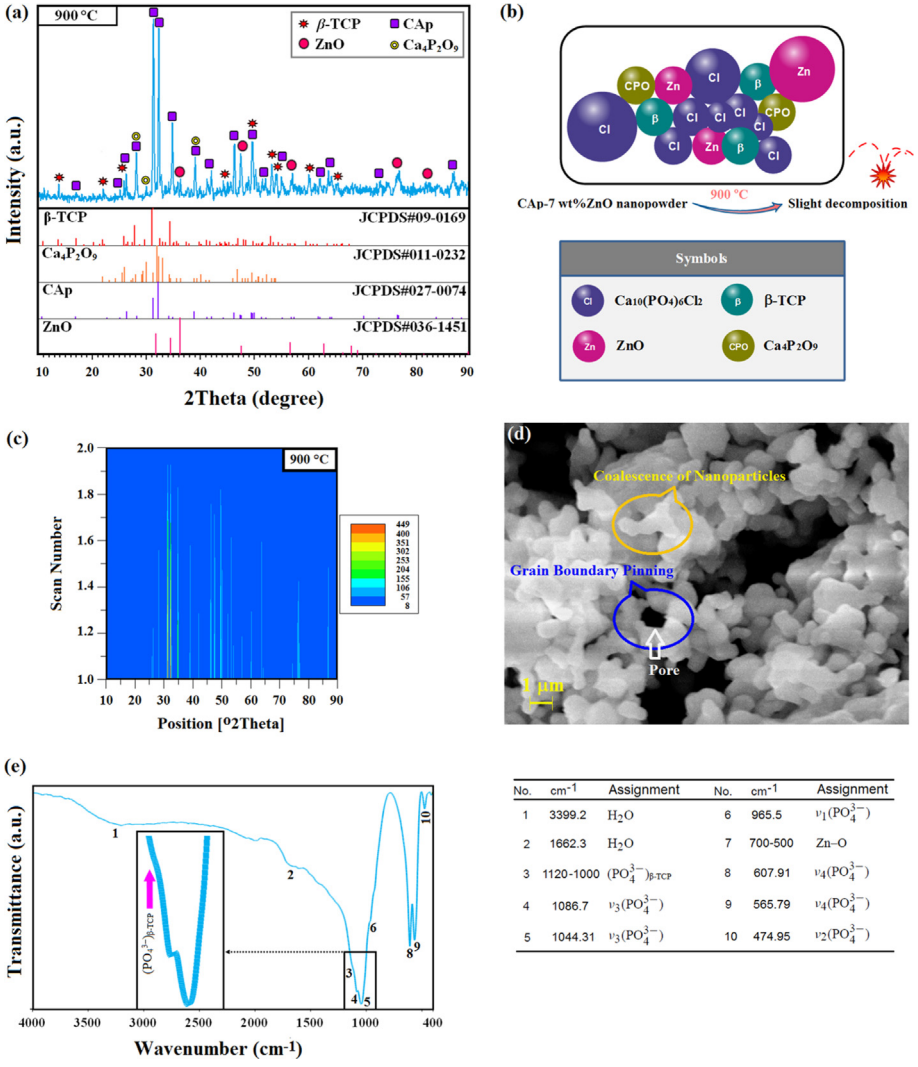

No.	cm-1	Assignment	No.	cm-1	Assignment
1	3399.2	H_2O	6	965.5	$\nu_1(PO_4^{3-})$
2	1662.3	H_2O	7	700-500	Zn–O
3	1120-1000	$(PO_4^{3-})_{\beta\text{-TCP}}$	8	607.91	$\nu_4(PO_4^{3-})$
4	1086.7	$\nu_3(PO_4^{3-})$	9	565.79	$\nu_4(PO_4^{3-})$
5	1044.31	$\nu_3(PO_4^{3-})$	10	474.95	$\nu_2(PO_4^{3-})$

Fig. 9. (a) XRD profile, (b) schematic view, (c) isolines view, (d) SEM image, and (e) FT-IR spectrum of CAp–ZnO composite nanopowder after thermal treatment at 900 °C for 1 h.

reaction:

$$Ca_{10}(PO_4)_6Cl_2 + H_2O \rightarrow 2\beta - Ca_3(PO_4)_2 + Ca_4P_2O_9 + 2HCl \quad (3)$$

As shown in the schematic view in Fig. 9b, the phase compositions were CAp, β-TCP, $Ca_4P_2O_9$, and ZnO after thermal treatment at 900 °C. Isolines plot of the heat treated composite nanopowder showed that the overlapping range of all scan data was very low which confirmed the formation of a high crystalline composite (Fig. 9c). According to the obtained data, the fraction of crystalline phase increased dramatically to $96 \pm 3\%$ after annealing at 900 °C. Moreover, at 900 °C, the lattice strain declined sharply to 0.0004 ± 0.000012, while the crystallite size rose significantly to 77 ± 2 nm. After heating, the unit cell volume of CAp declined considerably to 1607.5669 $Å^3$. This variation in unit cell volume can probably be attributed to the ion exchange reaction between CAp and ZnO during annealing. The ionic radius of Zn^{2+} is about 0.074 nm; that of calcium is about 0.1 nm [37]. Hence, this reaction led to a significant reduction in unit cell volume of CAp. The SEM image of CAp–7 wt% ZnO composite nanopowder after annealing at 900 °C is shown in Fig. 9d. It is obvious that the coalescence of nanoparticles with a mean size of 300 nm was dominant. In addition, significant growth of nanoparticles which usually happens through grain boundary migration was inhibited due to the grain boundary pinning by the network of open pores during heating at 900 °C [38]. Fig. 9e shows the FT-IR spectrum of CAp–ZnO composite nanopowder after annealing at 900 °C. Similar to the milled sample, the absence of the bands at 630 and 3568 cm^{-1} and the manifestation of a broad band at 750–730 cm^{-1} confirmed the formation of CAp [33]. The stretching vibration of the Zn–O appeared as a broad band in the range of 700–500 cm^{-1} [34]. At 900 °C, the bands at 1086.7 and 1044.31 cm^{-1} ascribed to ν_3 PO_4, the band at 965.5 attributed to ν_1 PO_4, the bands at 607.91 and 565.79 cm^{-1} belonged to ν_4 PO4, and the band at 474.95 cm^{-1} stems from ν_2 vibration of the PO_4^{3-} group [31]. Furthermore, the appearance of a broad band at 1120–1000 cm^{-1} belonging to the vibration of PO_4^{3-} group in β-TCP showed a slight decomposition of CAp after annealing at 900 °C [39].

4. Conclusions

The effect of ZnO content on the formation of Cap-based composite nanopowders via a novel facile mechanochemical process was investigated. The results showed that with the addition of 4 and 7 wt% ZnO, milling for 5 h resulted in the formation CAp–ZnO composite nanopowders. When the ZnO content reached 10 wt%, CAp–ZnO composite was not formed due to improper stoichiometric ratio of the reactants. In the presence of 4 wt% ZnO, the crystallite size reached a maximum of 57 ± 3 nm. In contrast, the lattice strain declined dramatically to 0.0014 ± 0.00007. In addition, the milled sample in the presence of 4 wt% ZnO had the highest degree of crystallinity ($87 \pm 4\%$) among the specimens. According to SEM and TEM images, the mean particle size of the mechanosynthesized composite nanopowder with ellipse-like and polygonal morphologies was about 98 nm. During annealing at 900 °C, the thermally induced crystallization resulted in the formation of a high crystalline composite nanopowder. The coalescence of nanoparticles with a mean size of 300 nm was dominant after annealing at 900 °C. The unit cell volume of CAp declined considerably after thermal treatment due to the ion exchange reaction between CAp and ZnO.

Acknowledgment

The authors are grateful to research affairs of Islamic Azad University, Najafabad Branch for supporting of this research.

References

[1] L.L. Hench, Bioceramics from concept to clinic, J. Am. Ceram. Soc. 74 (1991) 1487–1510.
[2] D.M. Liu, Q. Yang, T. Troczynski, W.J. Tseng, Structural evolution of sol–gel-derived hydroxyapatite, Biomaterials 23 (2002) 1679–1687.
[3] Y. Chen, X. Miao, Thermal and chemical stability of fluorohydroxyapatite ceramics with different fluorine contents, Biomaterials 26 (2005) 1205–1210.
[4] X. Bai, K. More, C.M. Rouleau, A. Rabiei, Functionally graded hydroxyapatite coatings doped with antibacterial components, Acta Biomater. 6 (2010) 2264–2273.
[5] M. Okada, T. Furuzono, Hydroxylapatite nanoparticles: fabrication methods and medical applications, Sci. Technol. Adv. Mater. 13 (2012) 1–14.
[6] S.J. Kalita, A. Bhardwaj, H.A. Bhatt, Nanocrystalline calcium phosphate ceramics in biomedical engineering, Mater. Sci. Eng. C 27 (2007) 441–449.
[7] S. Kannan, J.H.G. Rocha, J.M.F. Ferreira, Synthesis of hydroxychlorapatites solid solutions, Mater. Lett. 60 (2006) 864–868.
[8] M.H. Fathi, E. Mohammadi Zahrani, Mechanical alloying synthesis and bioactivity evaluation of nanocrystalline fluoridated hydroxyapatite, J. Cryst. Growth 311 (2009) 1392–1403.
[9] R. Ebrahimi-Kahrizsangi, B. Nasiri-Tabrizi, A. Chami, Characterization of single-crystal fluorapatite nanoparticles synthesized via mechanochemical method, Particuology 9 (2011) 537–544.
[10] P.H. Schlesinger, H.C. Blair, S.L. Teitalbaum, J.C. Edwards, Characterization of the osteoclast ruffled border chloride channel and its role in bone resorption, J. Biol. Chem. 272 (1997) 18636–18643.
[11] J.C. Rendón-Angeles, K. Yanagisawa, N. Ishizawa, S. Oishi, Effect of metal ions of chlorapatites on the topotaxial replacement by hydroxyapatite under hydrothermal conditions, J. Solid State Chem. 154 (2000) 569–578.
[12] B. Nasiri-Tabrizi, A. Fahami, R. Ebrahimi-Kahrizsangi, Phase transitions and structural changes of nanostructured chlorapatite under thermal treatment, Ceram. Int. (2013)http://dx.doi.org/10.1016/j.ceramint.2013.06.085.
[13] S.H. Rhee, Synthesis of hydroxyapatite via mechanochemical treatment, Biomaterials 23 (2002) 1147–1152.
[14] P. Honarmandi, P. Honarmandi, A. Shokuhfar, B. Nasiri-Tabrizi, R. Ebrahimi-Kahrizsangi, Milling media effects on synthesis, morphology and structural characteristics of single crystal hydroxyapatite nanoparticles, Adv. Appl. Ceram. 109 (2010) 117–122.
[15] K. Ioku, M. Yoshimura, S. Sōmiya, Microstructure and mechanical properties of hydroxyapatite ceramics with zirconia dispersion prepared by post-sintering, Biomaterials 11 (1990) 57–61.
[16] S. Nath, A.K. Dubey, B. Basu, Mechanical properties of novel calcium phosphate–mullite biocomposites, J. Biomater. Appl. 27 (2012) 67–78.
[17] R.J. Kane, R.K. Roeder, Effects of hydroxyapatite reinforcement on the architecture and mechanical properties of freeze-dried collagen scaffolds, J. Mech. Behav. Biomed. Mater. 7 (2012) 41–49.

[18] A.C. Tas, S.B. Bhaduri, S. Jalota, Preparation of Zn-doped β-tricalcium phosphate (β-$Ca_3(PO_4)_2$) bioceramics, Mater. Sci. Eng.: C 27 (2007) 394–401.
[19] M. Hambidge, R.J. Cousins, R.B. Costello, Zinc and health: current status and future directions, J. Nutr. 130 (2000) 1341S–1343S.
[20] G. Oner, B. Bhaumick, R.M. Bala, Effect of zinc deficiency on serum somatomedin levels and skeletal growth in young rats, Endocrinology 114 (1984) 1860–1863.
[21] K. Cheng, Z. Guan, W. Weng, H. Wang, J. Lin, P. Du, G. Han, Hydroxyapatite/ZnO-nanorod composite coatings with adjustable hydrophilicity and Zn release ability, Thin Solid Films 544 (2013) 260–264, http://dx.doi.org/10.1016/j.tsf.2013.03.108.
[22] C. Suryanarayana, Mechanical alloying and milling, Prog. Mater. Sci. 46 (2001) 1–184.
[23] F. Sun, F.H.S. Froes, Synthesis and characterization of mechanical-alloyed Ti_xMg alloys, J. Alloys Compd. 340 (2002) 220–225.
[24] S.S. Rayalu, J.S. Udhoji, S.U. Meshram, R.R. Naidu, S. Devotta, Estimation of crystallinity in flyash-based zeolite-A using XRD and IR spectroscopy, Curr. Sci. 89 (2005) 2147–2151.
[25] J. Qian, Y. Kang, W. Zhang, Zh. Li, Fabrication, chemical composition change and phase evolution of biomorphic hydroxyapatite, J. Mater. Sci.: Mater. Med. 19 (2008) 3373–3383.
[26] W.F. Smith, J. Hashemi, Foundations of materials science and engineering, Crystal Structures and Crystal Geometry, McGraw-Hill Science, New York, 2004, p. 67–115.
[27] X'Pert High Score, Version 1.0d, PANalytical B.V. Almelo, The Netherlands.
[28] B. Nasiri-Tabrizi, A. Fahami, Crystallization behavior of nanostructured amorphous tricalcium phosphate under thermal treatment, Mater. Lett. 106 (2013) 396–400.
[29] B. Nasiri-Tabrizi, P. Honarmandi, R. Ebrahimi-Kahrizsangi, P. Honarmandi, Synthesis of nanosize single-crystal hydroxyapatite via mechanochemical method, Mater. Lett. 63 (2009) 543–546.
[30] S. Kannan, A. Rebelo, A.F. Lemos, A. Barba, J.M.F. Ferreira, Synthesis and mechanical behaviour of chlorapatite and chlorapatite/β-TCP composites, J. Eur. Ceram. Soc. 27 (2007) 2287–2294.
[31] B. Nasiri-Tabrizi, A. Fahami, Reaction mechanisms of synthesis and decomposition of fluorapatite–zirconia composite nanopowders, Ceram. Int. 39 (2013) 5125–5136.
[32] M.M. Seckler, M. Danese, S. Derenzo, J.V. Valarelli, M. Giulietti, R. Rodriguez-Clemente, Influence of process conditions on hydroxyapatite crystallinity obtained by direct crystallization, J. Mater. Res. 2 (1999) 59–62.
[33] I. Nikcevic, V. Jokanovic, M. Mitric, Z. Nedic, D. Makovec, D. Uskokovic, Mechanochemical synthesis of nanostructured fluorapatite/fluorhydroxyapatite and carbonated fluorapatite/fluorhydroxyapatite, J. Solid State Chem. 177 (2004) 2565 − 2574.
[34] J.H. Chen, C.Y. Cheng, W.Y. Chiu, C.F. Lee, N.Y. Liang, Synthesis of ZnO/polystyrene composites particles by Pickering emulsion polymerization, Eur. Polym. J. 44 (2008) 3271–3279.
[35] J.P. Lafon, E. Champion, D. Bernache-Assollant, Processing of AB-type carbonated hydroxyapatite $Ca_{10-x}(PO_4)_{6-x}(CO_3)_x(OH)_{2-x-2y}(CO_3)_y$ ceramics with controlled composition, J. Eur. Ceram. Soc. 28 (2008) 139 − 147.
[36] P. Balaz, Mechanochemistry in Nanoscience and Minerals Engineering, 1st ed., Springer, Berlin, Heidelberg, 2008.
[37] D.G. Peiffer, B.L. Hager, R.A. Weiss, P.K. Agarwal, R.D. Lundberg, J. Polym. Sci.: Polym. Phys. Ed. 23 (1985) 1869–1881.
[38] E. Champion, Sintering of calcium phosphate bioceramics, Acta Biomater. 9 (2013) 5855–5875.
[39] I. Cacciotti, A. Bianco, High thermally stable Mg-substituted tricalcium phosphate via precipitation, Ceram. Int. 37 (2011) 127–137.